

Computational insights on drug effects on intrinsic stochasticity of mouse pacemaker cell activity

Nitay Aspis,¹ Ido Weiser-Bitoun,^{1,2} and Yael Yaniv^{1,*}

¹Laboratory of Bioelectric and Bioenergetic Systems, Faculty of Biomedical Engineering, Technion-IIT, Haifa, Israel and ²Department of Internal Medicine "C", Rambam Health Care Campus, Haifa, Israel

ABSTRACT In sinoatrial node cells (SANCs), stochastic Ca^{2+} release from the sarcoplasmic reticulum (SR) interacts with membrane channels, inducing their stochastic opening and closing, leading to interbeat interval (IBI) variability (BIV). Additionally, stochastic neurotransmitter release activates cAMP/protein kinase A signaling, influencing membrane channels and SR proteins, further contributing to BIV. Most computational models produce deterministic IBIs, lacking physiological BIV. We tested three hypotheses: 1) incorporating stochastic behavior into intrinsic mechanisms mimics experimental BIV, 2) increased neurotransmitter stimulation via β -adrenergic receptor (β -AR) activation, phosphodiesterase (PDE) inhibition, or enhanced sarco/endoplasmic reticulum Ca^{2+} -ATPase (SERCA) activity shortens IBIs and reduces BIV, and 3) these interventions affect BIV parameters differently at short and long timescales. To test this, we introduced the stochastic behavior of Ca^{2+} channels, ryanodine receptor (RyR), funny channel, and autonomic nervous system signaling via carbachol and isoproterenol (ISO) stimulations into our mouse coupled-clock SANC model. Kolmogorov-Smirnov tests showed that the IBI distribution of our stochastic model aligns significantly more closely with experimental data than those of the deterministic model. RyR noise maximized BIV, mainly increasing short-scale (1–10) entropy (IBI irregularity). Funny channel noise influenced short-scale entropy and low-frequency power, whereas ISO noise affected long-scale (11–20) entropy. Augmented β -AR activation or PDE inhibition shortened the IBI and reduced its standard deviation, mirroring SERCA activity enhancement. β -AR activation reduced low-frequency power, PDE inhibition decreased entropy across scales, and SERCA activation reduced power in all frequency bands. Thus, interactions among intrinsic stochastic mechanisms contribute to BIV complexity, and drug effects have different responses on BIV.

SIGNIFICANCE The heart's natural pacemaker, the sinoatrial node, relies on complex interactions between ion channels and intracellular signaling to regulate heartbeat timing. However, existing computational models fail to replicate the natural variability seen in experimental data. Our study introduces stochastic mechanisms into a computational model of sinoatrial node cells, successfully reproducing physiological beat interval variability (BIV). We show that different sources of noise— Ca^{2+} release, ion channel fluctuations, and autonomic signaling—affect BIV at distinct timescales. Furthermore, pharmacological interventions targeting β -adrenergic signaling, phosphodiesterase activity, and Ca^{2+} cycling alter BIV in unique ways. These findings enhance our understanding of cardiac pacemaker variability and may guide the development of treatments for heart rhythm disorders.

INTRODUCTION

Drug development is an esteemed task that requires consideration of possible interactions of the drug with various body systems (1). Given that the cardiovascular system interacts with many organs, testing the effects of drugs on cardiac activity, specifically its rhythm, is essential. Both short- and long-term changes in cardiac rhythm manifest as heart

rate variability (HRV) and mean heart rate (2). Alterations in HRV have been correlated with changes in nervous system and key channel activities, affecting cardiac activity and drug interactions (3).

An approach commonly used to examine the effect of drugs on cardiovascular rhythm focuses on the mechanisms governing the activity of sinoatrial node (SAN) pacemaker cells (SANCs), which comprise the heart's main pacemaker. SAN activity is regulated by a coupled-clock system, which involves a complex interaction between the sarcoplasmic reticulum (SR) and the membrane channels (4). At the core of this regulatory framework are spontaneous

Submitted March 7, 2025, and accepted for publication July 25, 2025.

*Correspondence: yaely@bm.technion.ac.il

Editor: Jeffrey J. Saucerman.

<https://doi.org/10.1016/j.bpj.2025.07.031>

© 2025 Biophysical Society. Published by Elsevier Inc.

All rights are reserved, including those for text and data mining, AI training, and similar technologies.



local Ca^{2+} releases from the SR via ryanodine receptors (RyRs) and reuptake by the sarco/endoplasmic reticulum Ca^{2+} -ATPase (SERCA) (5).

The stochastically released Ca^{2+} from the SR interacts with the $\text{Na}^+/\text{Ca}^{2+}$ exchanger, influencing membrane potential (6) together with stochastic fluctuations in ion channel activity (7). These fluctuations introduce variability in action potential (AP) duration, which is quantified by the inter-beat interval (IBI). Experimental evidence has demonstrated variability in the IBI, also known as beat interval variability (BIV), in single SANCs (8,9), representing the single-cell analog to whole-heart HRV.

In parallel to the coupled-clock mechanisms, stochastic release of neurotransmitters activates adenylyl cyclase (AC)-cAMP/protein kinase A (PKA) signaling, which also interacts with membrane channels, RyR, and SERCA proteins (4). This AC-cAMP/PKA signaling can also be intrinsically activated by Ca^{2+} , whereas cAMP degradation by phosphodiesterase (PDE) is tightly controlled by intrinsic signaling, such as Ca^{2+} and PKA (10). The interaction between intrinsic mechanisms and neurotransmitters affects both short- and long-range HRV *in vivo* (11).

Computational modeling is an important tool for exploring the effects of drugs and mutations on SANC functions. Traditionally, computational models of SANC activity include a detailed description of the coupled-clock system, providing deterministic outcomes that often overlook the variability in SANC behavior and its impact on the IBI (12). Seminal work has included the stochastic behavior of SANC IBIs (13). However, they primarily focused on modulating the stochasticity of the action potential itself (output) rather than on the mechanisms that elicit the action potential. Furthermore, the nature of the stochasticity of each intrinsic mechanism and neurotransmitter differs. New generations of SANC models have also incorporated variability, but it was restricted to the Ca^{2+} clock (14), neglecting other important mechanisms that contribute to variability. This limitation has hindered our understanding of how drugs and mutations in certain molecules influence BIV. Fox et al. (15) demonstrated that noise arising from finite ion channel populations can be modeled as multiplicative white noise added to gating variables, with amplitude derived from the underlying transition rates. This approach provides a biophysically grounded framework for simulating intrinsic channel noise at the single-cell level. In addition, Rosenberg et al. (16) analyzed in our lab the beat-to-beat variability of SAN activity in canine tissue and found that autonomic influences exhibit structured spectral characteristics, with low-frequency (LF) components associated with sympathetic modulation and high-frequency (HF) components reflecting parasympathetic activity.

To gain mechanistic insights into the effect of the stochastic behavior of the intrinsic mechanism on BIV, we incorporated the stochastic behavior of the Ca^{2+} channels, the RyR channel, the funny current (I_f) channel, and the autonomic

nervous system (ANS) via carbachol (CCh) and isoproterenol (ISO) stimulations into our mouse coupled-clock SANC model (17).

We hypothesized that 1) integrating stochastic behavior into intrinsic mechanisms will mimic experimental BIV; 2) increased neurotransmitter stimulation via increased β -adrenergic receptor (β -AR) activation, inhibition of PDE, or increased SERCA activity will shorten the IBI and reduce BIV; and 3) these drugs/mutations have distinct effects on BIV parameters in long and short scales.

MATERIALS AND METHODS

Our proposed stochastic model utilizes our previously published deterministic model of the mouse SANC (12) (which was informed by the models developed by Kharche et al. (18), Yaniv et al. (19), and Behar et al. (20)) to simulate the physiological activity of a single spontaneously beating SANC. Only the modifications and the new assumptions introduced are detailed herein.

To model intrinsic physiological variability in SAN cell dynamics, we incorporated stochasticity into the gating equations of selected membrane and intracellular ion channels using a Langevin-type formalism. For each gating variable governed by forward (α) and backward (β) rates, we added a noise term proportional to $\sqrt{\alpha(1-x)+\beta x}$, where x represents the gating variable. This term captures fluctuations arising from the finite number of ion channels. Our approach builds on the stochastic extension of the Hodgkin-Huxley framework proposed by Fox et al. (15) and was implemented numerically using the Euler-Maruyama method, which is appropriate for integrating stochastic differential equations with multiplicative noise. The noise term was scaled by the square root of the time step and a tunable amplitude factor, balancing physiological realism with numerical stability.

ANS variability, modulating β -adrenergic (ISO) and cholinergic (CCh) inputs, was modeled using spectrally shaped noise applied in the frequency domain. This approach was conceptually adapted from Rosenberg et al. (16), who simulated beat-to-beat variability in canine SAN tissue and identified distinct spectral peaks at approximately 0.15 and 0.35 Hz, corresponding to sympathetic and parasympathetic activity, respectively (see Fig. S1). To suit our single murine SAN cell model, we generated pink-colored noise with smoother spectral shaping and center frequencies at 0.04 (LF) and 0.15 (HF) Hz, reflecting species-specific differences. In this design, ISO fluctuations were enriched in LF content, whereas CCh fluctuations emphasized HF content, consistent with known physiological correlations between sympathetic activity and LF variability, and parasympathetic activity and HF variability (16).

Model assumptions

- 1) Given that SANCs are pivotal to the initiation of heart contractions, either the measurement or the simulation of action potentials within these cells can be representative of heartbeats, thereby enabling the calculation of IBI and BIV parameters.
- 2) BIV is significantly influenced by the stochastic nature of ion channels and SR involved in SANC activity. Thus, we incorporated specific noise into intrinsic state variables within the existing model rather than assuming global noise in the membrane action potential.
- 3) The overall stochastic behavior of the SANC can be characterized by the sum of a finite number of physiological variables, with random noise derived from known distributions.
- 4) All BIV parameters—linear, nonlinear, and frequency—are crucial in depicting the stochastic behavior of the SANC and are instrumental for comparison with *in vitro* recordings.

- 5) Linear, nonlinear, and frequency analysis yielded 10 physiological parameters that primarily affect BIV: five distinct state variables of Ca^{2+} channels, three distinct state variables of the RyR channel, the funny channel, and the ANS function composed of parasympathetic and sympathetic stimulations via CCh and ISO, respectively. See the below description of all relevant state variables.
- 6) The number of channels per gating variable is assumed to be sufficiently large for the diffusion approximation, as described by Fox's Langevin formalism, to be valid.
- 7) The noise terms are modeled as zero-mean Gaussian processes, consistent with the central limit theorem for large channel populations.
- 8) A uniform noise amplitude constant is applied across all membrane-associated gating variables
- 9) All RyR-related gating variables are assigned a uniform, lower noise amplitude.
- 10) The stochastic differential equations are integrated using the Euler-Maruyama method with a sufficiently small time step to ensure numerical stability and accuracy.
- 11) ANS inputs fluctuate around fixed baseline concentrations, maintaining physiologically tonic levels.
- 12) Noise processes for different gating variables and autonomic signals are uncorrelated and independently generated.

The dynamics of the original model are described by a system of 42 ordinary differential equations. The code will be made accessible on our website upon publication at <https://bioelectric-bioenergetic-lab.net.technion.ac.il/> and on GitHub at <https://github.com/Bioelectric-and-Bioenergetic-Lab/Stochastic-SAN-simulation.git>. For details regarding constants and equation parameters, please refer to the **supporting material**. Initial conditions are provided in **Table S1**, model constants in **Table S2**, and detailed equations in **section S3** of the **supporting material**.

In the equations below, noise was incorporated into the Ca^{2+} channel state variables, the RyR state variables, the funny channel, and the concentrations of CCh and ISO.

The calcium channel activity is described by five state variables (fL12, dL12, fL13, dL13, and fCa). fL12 represents the inactivation gate variable for the L-type Ca^{2+} (I_{Cal}) channel 1.2, whereas dL12 represents the activation gate variable for this channel. Similarly, fL13 and dL13 represent the inactivation and activation gate variables for the I_{Cal} channel 1.3. fCa is the Ca^{2+} -dependent inactivation gating variable for both the 1.2 and 1.3 I_{Cal} channels.

$$dL12_{\text{inf}} = \frac{1}{1 + e^{\frac{-Vm+3}{5}}} \quad (1)$$

$$fL12_{\text{inf}} = \frac{1}{1 + e^{\frac{Vm+36}{4.6}}} \quad (2)$$

$$dL13_{\text{inf}} = \frac{1}{1 + e^{\frac{-Vm+13.5}{6}}} \quad (3)$$

$$fL13_{\text{inf}} = \frac{1}{1 + e^{\frac{Vm+35}{7.3}}} \quad (4)$$

$$fCa_{\text{inf}} = \frac{K_{mfCa}}{K_{mfCa} + Ca_{\text{sub}}} \quad (5)$$

$$\alpha_{dL12} = \frac{dL12_{\text{inf}}}{tau_{dL}} \quad (6)$$

$$\beta_{dL12} = \frac{1 - dL12_{\text{inf}}}{tau_{dL}} \quad (7)$$

$$noise_{dL12} = \sqrt{\alpha_{dL12} * (1 - dL12) + \beta_{dL12} * dL12}$$

$$* * membrane_{\text{noise}} * \sqrt{dt} \quad (8)$$

$$\alpha_{fL12} = \frac{fL12_{\text{inf}}}{tau_{fL}} \quad (9)$$

$$\beta_{fL12} = \frac{1 - fL12_{\text{inf}}}{tau_{fL}} \quad (10)$$

$$noise_{fL12} = \sqrt{\alpha_{fL12} * (1 - fL12) + \beta_{fL12} * fL12}$$

$$* * membrane_{\text{noise}} * \sqrt{dt} \quad (11)$$

$$\alpha_{dL13} = \frac{dL13_{\text{inf}}}{tau_{dL}} \quad (12)$$

$$\beta_{dL13} = \frac{1 - dL13_{\text{inf}}}{tau_{dL}} \quad (13)$$

$$noise_{dL13} = \sqrt{\alpha_{dL13} * (1 - dL13) + \beta_{dL13} * dL13}$$

$$* * membrane_{\text{noise}} * \sqrt{dt} \quad (14)$$

$$\alpha_{fL13} = \frac{fL13_{\text{inf}}}{tau_{fL}} \quad (15)$$

$$\beta_{fL13} = \frac{1 - fL13_{\text{inf}}}{tau_{fL}} \quad (16)$$

$$noise_{fL13} = \sqrt{\alpha_{fL13} * (1 - fL13) + \beta_{fL13} * fL13}$$

$$* * membrane_{\text{noise}} * \sqrt{dt} \quad (17)$$

$$\alpha_{fCa} = \frac{fCa_{\text{inf}}}{tau_{fCa}} \quad (18)$$

$$\beta_{fCa} = \frac{1 - fCa_{\text{inf}}}{tau_{fCa}} \quad (19)$$

$$\begin{aligned} noise_{fCa} &= \sqrt{\alpha_{fCa} * (1 - fCa) + \beta_{fCa} * fCa} \\ &\quad * * membrane_{noise} * \sqrt{dt} \frac{dfL12}{dt} \\ &= \frac{fL12_{inf} - fL12}{tau_{fL}} + noise_{fL12} \end{aligned} \quad (20)$$

$$\frac{dfL12}{dt} = \frac{dL12_{inf} - dL12}{tau_{dL}} + noise_{dL12} \quad (21)$$

$$\frac{dfL13}{dt} = \frac{fL13_{inf} - fL13}{tau_{fL}} + noise_{fL13} \quad (22)$$

$$\frac{ddL13}{dt} = \frac{dL13_{inf} - dL13}{tau_{dL}} + noise_{dL13} \quad (23)$$

$$\frac{dfCa}{dt} = \frac{fCa_{inf} - fCa}{tau_{fCa}} + noise_{fCa} \quad (24)$$

V_m is the membrane voltage, tau_{dL} , tau_{fL} , and tau_{fCa} are the time constants for dL, fL, and fCa variables, respectively. K_{mfCa} is the dissociation constant of Ca^{2+} -dependent inactivation of I_{CaL} , and Ca_{sub} is the Ca^{2+} concentration in the subspace. $membrane_{noise}$ is a Gaussian noise with zero mean and an SD of 10^{-3} , and dt is the timestep.

The RyR activity is described by 4 states (R, S, OO, and RI). R represents the fraction of reactivated (closed) RyR channels, S is the inactive-state fraction of RyR, OO is the open-state fraction of RyR, and RI represents the fraction of inactivated RyR channels:

$$\alpha_R = k_{im} \cdot RI + k_{om} \cdot OO \quad (25)$$

$$\beta_R = k_{iSRCa} \cdot [Ca^{2+}]_{sub} \cdot R + k_{oSRCa} \cdot [Ca^{2+}]_{sub}^2 \cdot R \quad (26)$$

$$noise_R = \sqrt{\alpha_R + \beta_R} * RyR_{noise} * \sqrt{dt} \quad (27)$$

$$\alpha_{RI} = k_{om} \cdot S + k_{iSRCa} \cdot [Ca^{2+}]_{sub} \cdot R \quad (28)$$

$$\beta_{RI} = k_{oSRCa} \cdot [Ca^{2+}]_{sub}^2 \cdot RI + k_{im} \cdot RI \quad (29)$$

$$noise_{RI} = \sqrt{\alpha_{RI} + \beta_{RI}} * RyR_{noise} * \sqrt{dt} \quad (30)$$

$$\alpha_S = k_{iSRCa} \cdot [Ca^{2+}]_{sub} \cdot OO + k_{oSRCa} \cdot [Ca^{2+}]_{sub}^2 \cdot RI \quad (31)$$

$$\beta_S = k_{im} \cdot S + k_{om} \cdot S \quad (32)$$

$$noise_S = \sqrt{\alpha_S + \beta_S} * RyR_{noise} * \sqrt{dt} \quad (33)$$

$$\begin{aligned} \frac{dR}{dt} &= (k_{im} \cdot RI - k_{iSRCa} \cdot [Ca^{2+}]_{sub} \cdot R) \\ &\quad - (k_{oSRCa} \cdot [Ca^{2+}]_{sub}^2 \cdot R - k_{om} \cdot OO) \\ &\quad + noise_R \end{aligned} \quad (34)$$

$$\begin{aligned} \frac{dRI}{dt} &= (k_{om} \cdot S - k_{oSRCa} \cdot [Ca^{2+}]_{sub}^2 \cdot RI) \\ &\quad - (k_{im} \cdot RI - k_{iSRCa} \cdot [Ca^{2+}]_{sub} \cdot R) \\ &\quad - noise_R \end{aligned} \quad (35)$$

$$\begin{aligned} \frac{dS}{dt} &= (k_{iSRCa} \cdot [Ca^{2+}]_{sub} \cdot OO - k_{im} \cdot S) \\ &\quad - (k_{om} \cdot S - k_{oSRCa} \cdot [Ca^{2+}]_{sub}^2 \cdot RI) \\ &\quad + noise_S \end{aligned} \quad (36)$$

$$\frac{dOO}{dt} = 0 - dR - dRI - dS \quad (37)$$

k_{oSRCa} and k_{iSRCa} are the SERCA rate transition constants, and k_{om} and k_{im} are the RyR rate transition constants. $noise_R$ and $noise_S$ are the noise parameters added to each RyR state variable. Distinct noise was added to the RI, S, and R state variables. RyR_{noise} is a Gaussian noise with zero mean and an SD of 10^{-5} , and dt is the timestep.

The hyperpolarization-activated funny current (HCN_4), I_f , is described by

$$\begin{aligned} V_{shift} &= K_{if} \cdot [\text{cAMP}]^{n_{if}} / (K_{0.5if}^{n_{if}} + [\text{cAMP}]^{n_{if}}) \\ &\quad - 18.1040, \end{aligned} \quad (38)$$

$$y_{inf} = 1 / (1 + \exp((V_m + 104.2 - V_{shift}) / 16.3)), \quad (39)$$

$$\begin{aligned} tau_y &= 1.5049 / (\exp(-(V_m + 590.3) \cdot 0.01094) \\ &\quad + \exp((V_m - 85.1) / 17.2)), \end{aligned} \quad (40)$$

$$\alpha_y = \frac{y_{inf}}{tau_y}, \quad (41)$$

$$\beta_y = \frac{1 - y_{inf}}{tau_y}, \quad (42)$$

$$\begin{aligned} noise_y &= \sqrt{\alpha_y * (1 - y) + \beta_y * y * membrane_{noise}} \\ &\quad * \sqrt{dt}, \text{ and} \end{aligned} \quad (43)$$

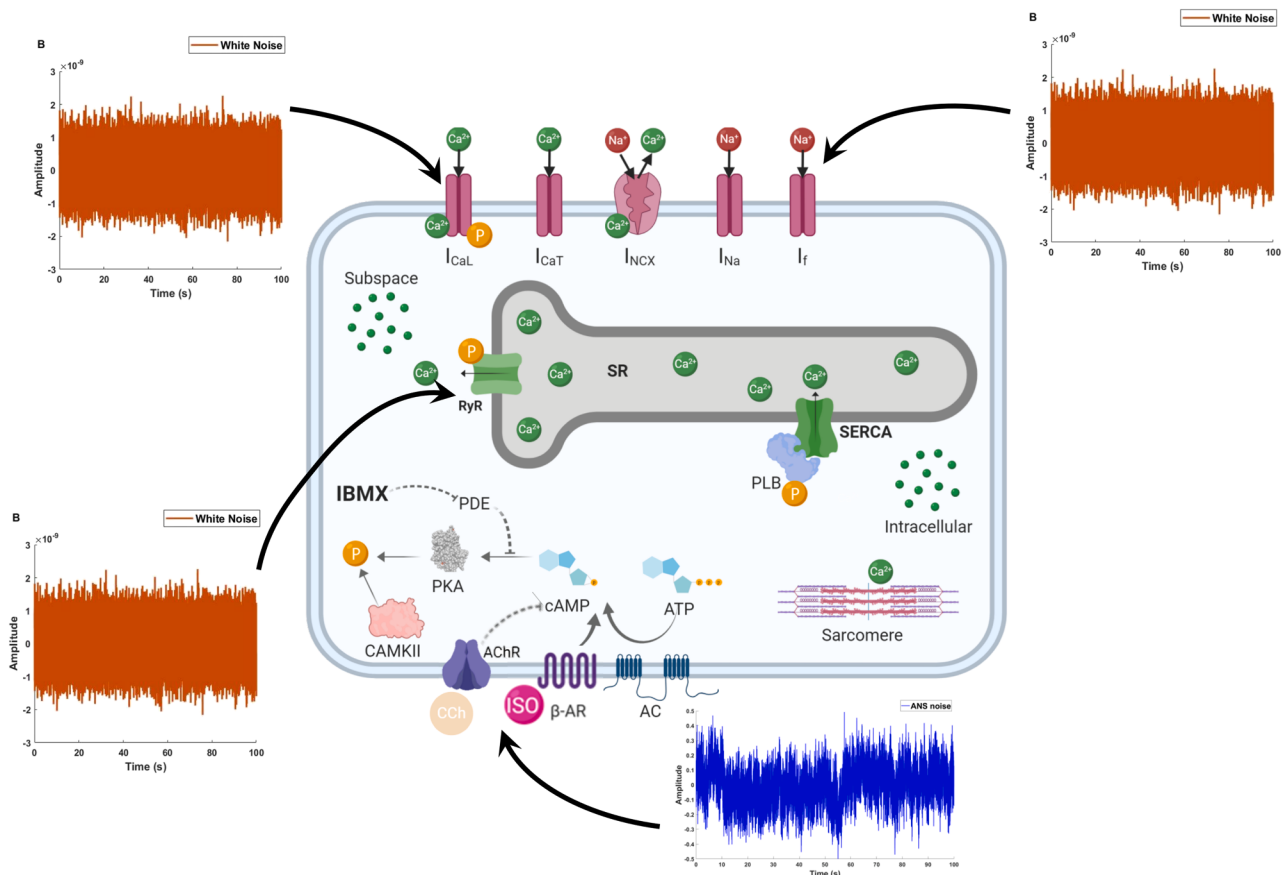


FIGURE 1 A schematic description of the stochastic sinoatrial node cell model, which includes the interplay between β -adrenergic receptors (β -ARs), nicotinic acetylcholine receptors (AChRs), adenyl cyclase (AC), phosphodiesterase (PDE) activity, and cAMP/protein kinase A (PKA)-dependent signaling to myofilaments, sarcoplasmic reticulum (SR) Ca^{2+} cycling proteins, and ion channels in the sinoatrial node cell. Four sources of noise were incorporated: 1) white noise, which has a zero mean and an SD of 10^{-3} , applied to five state variables of the Ca^{2+} L-type channel; 2) white noise with zero mean and an SD of 10^{-3} was applied to a single state variable of the funny current channel; 3) white noise with zero mean and an SD of 10^{-5} was applied to three state variables of the ryanodine receptor (RyR); and 4) masked pink noise with a power spectral density that decreases by 3 dB per octave was applied to isoproterenol (ISO) and carbachol (CCh) concentrations, with an enriched low-frequency (LF) band or an enriched high-frequency (HF) band, respectively.

$$\frac{dy}{dt} = \text{noise}_y + (y_{\text{inf}} - y) / \tau_y, \quad (44)$$

where K_{if} , $K_{0.5if}$, and n_{if} are the funny current channel rate transition constants and V_m is the membrane potential. noise_y is the noise that was added to the funny current channel activation gating variable. membrane_{noise} is a Gaussian noise with zero mean and an SD of 10^{-3} , and dt is the timestep.

ANS variability was introduced directly through the ISO and CCh concentrations.

$$\text{noise}_{ISO}(f) = \text{pink}(f) * M_{ISO}(f) \quad (45)$$

$$\text{noise}_{CCh}(f) = \text{pink}(f) * M_{CCh}(f) \quad (46)$$

$$ISO = ISO_0 + \text{noise}_{ISO} \quad (47)$$

$$CCh = CCh_0 + \text{noise}_{CCh} \quad (48)$$

ISO_0 and CCh_0 are the mean base ISO and CCh concentrations, respectively. $\text{pink}(f)$ is a unit-variance pink noise, and $M(f)$ is a smooth mask function controlling the LF/HF emphasis, with ISO enriched in the LF band (0.04–0.15 Hz) and CCh enriched in the HF band (>0.15 Hz).

Model design

For the purpose of analyzing BIV parameters from the model output, we used a $10-\mu\text{s}$ timestep and evaluated the results of a 3-min simulation. To avoid transient responses affecting the results, we removed the first 20 s of the model. Considering the rapid heartbeats of the mouse model (over 5 beats per second), the remaining 160 s were sufficient for the calculation of very LFs, along with other BIV parameters.

We analyzed the impact of inserted noise on each variable independently. By subtracting the original deterministic output of each variable from the output in the noisy model, after introducing noise to only the examined variable, the noise was isolated and evaluated. Subsequently, we analyzed its frequencies and linear and nonlinear statistics to ascertain if the expected noise characteristics were achieved.

To evaluate the cumulative impact of all inserted noises, we extracted the membrane voltage (V_m) from each model iteration. Subsequently, we identified the peaks representing action potentials and subsequent heartbeats and calculated the IBI as the time difference in milliseconds between consecutive peaks. Each IBI vector was analyzed and compared with in vivo recordings across several dimensions: statistical (SD and mean), linear analysis (histogram), nonlinear analysis (Poincaré plot and multiscale entropy [MSE]), and frequency analysis (power spectrum density [PSD]). These analyses were carried out using MATLAB and PhysioZoo, a specialized HRV analysis software (21).

We refined the model by identifying the most relevant variables and assessing their collective impact in comparison to mouse SANC recordings. The final model configuration was determined by comparing all BIV parameters in the stochastic model with those in the SANC recordings. We empirically established the optimal combination of variables, noise types, and noise intensities (refer to Fig. 1).

After finalizing the model, it was used to assess the effects of various drugs previously simulated in the original model on BIV. The outcomes were compared with those reported in the literature.

Statistical analysis

The output of the final model was compared to experimental data from recordings of five mouse SANCs. Each model configuration was simulated 10 times to calculate 95% two-sided confidence intervals and SD for each parameter. The KST was employed to assess the congruence between the IBI distributions of the original deterministic model and the experimental recordings, as well as between our stochastic model and the experimental recordings. The resulting statistics were compared using a permutation test under the null hypothesis that no significant difference exists between the two KST-derived congruences.

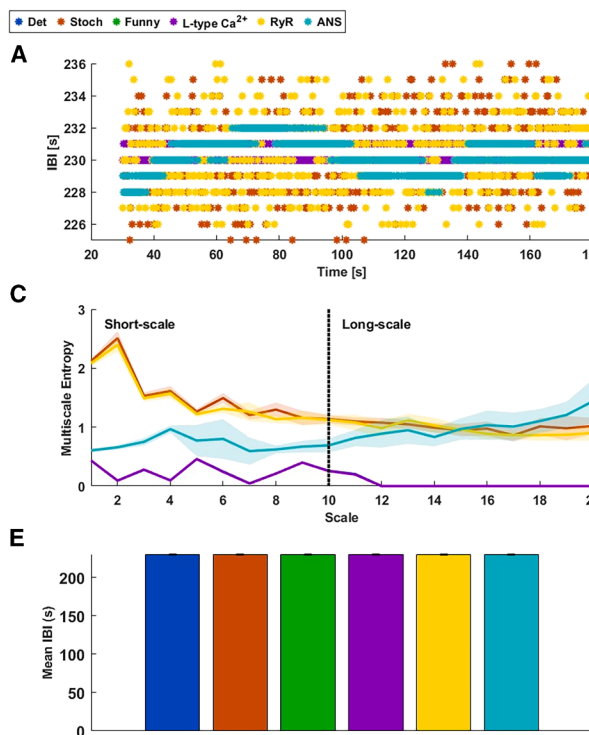


FIGURE 2 Incorporation of random noise into distinct variables separately. (A) A representative sample from each stochastic model, showing the calculated inter-beat intervals (IBIs). (B) Mean histograms of all models with 95% two-sided confidence intervals. (C) Multiscale entropy analysis of both models with 95% two-sided confidence intervals. (D) Power spectral density analysis across all frequencies with 95% two-sided confidence intervals. (E) The mean IBI derived from each model, with error bars representing ± 1 standard deviation. (F) The coefficient of variance of the IBIs, also shown with error bars indicating ± 1 standard deviation.

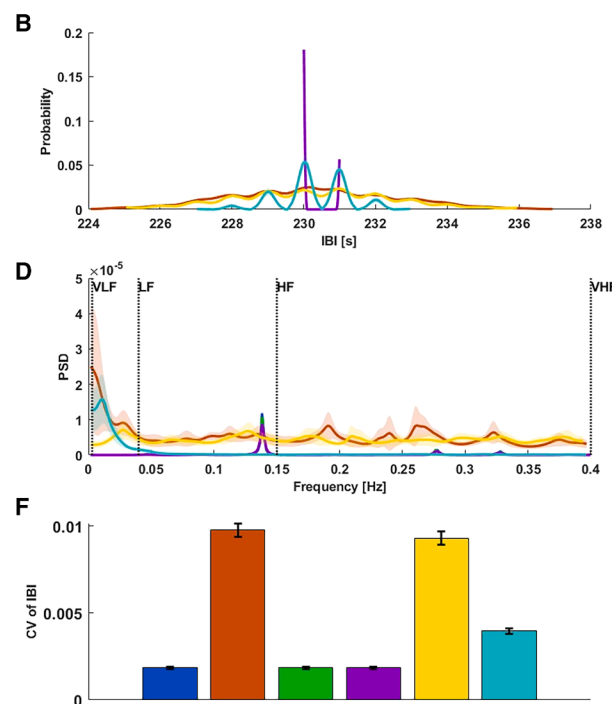
RESULTS

Noise inserted into V_m

Initially, we aimed to simulate stochasticity conditions similar to those reported by Dvir et al. (13). To this end, we introduced white noise into the membrane voltage (V_m). Fig. S2 provides a basic comparison of different types of noise: white noise, which represents a Gaussian noise signal with a flat power spectral density across all frequencies; brown noise, which has a power spectral density that decreases by 6 dB per octave; and pink noise, which decreases by 3 dB per octave. Fig. S3 illustrates the distinct effects of each noise on the BIV. Whereas the membrane potential remained nearly unchanged (Fig. S3 A), the IBI distribution varied (Fig. S3 B), as evidenced in the Poincaré plot (Fig. S3 C) and histogram (Fig. S3 D). The MSE was relatively similar across all noise types (Fig. S3 E), but their PSDs differed significantly (Fig. S3 F), with stochastic V_m using brown noise producing the highest PSD and pink noise the lowest across all frequencies.

Noise inserted into different physiological state variables

We incorporated noise into 10 physiological state variables: 1) five state variables describing Ca²⁺ channel activity—fL12 and dL12 for the L-type Ca²⁺ channel 1.2 inactivation and



activation gate variables, respectively; fL13 and dL13 for the L-type Ca^{2+} channel 1.3 inactivation and activation gate variables, respectively; and fCa for the Ca^{2+} -dependent inactivation gating variable; 2) three state variables describing the ryanodine function—R for the reactivation fraction, S for the inactive-state fraction, and RI for the fraction of inactivated RyR channels; 3) activation fraction of the funny channel; and 4) concentrations of stimulations representing the ANS function—ISO and CCh for the stimulation of the sympathetic and parasympathetic systems, respectively. We tested the effect of each noise source individually and together on BIV.

Fig. 2 illustrates that each stochastic variable had a distinct effect on the BIV, whereas the accumulated influence was reflected in the total stochastic model. The stochastic ryanodine contributed the most to the total variance and short-scale entropy, whereas the ANS stochasticity primarily affected LFs and long-scale entropy. The influence of Ca^{2+} channel and funny channel variables was more moderate. The noise effect was not additive, but rather synergistic.

Comparison between the deterministic and our stochastic model

After analyzing each stochastic component separately, we compared the overall stochastic model, which included noise

added to nine of its state variables, as well as stochasticity introduced via simulated ANS stimulation using ISO and CCh, corresponding to sympathetic and parasympathetic stimulation, respectively. **Fig. 3 A** shows a representative membrane potential for both the deterministic and stochastic models, and **Fig. 3 B** presents the calculated IBI from the same representative sample. **Fig. 3 C** illustrates the Poincaré plot for this sample. **Fig. 3 D** shows histograms from all simulations of both models, along with 95% two-sided confidence intervals, demonstrating a significant increase in IBI distribution variability in the stochastic model. In the deterministic model, the very narrow fluctuations stem from numerical instability caused by the accumulation of truncation and round-off errors in the MATLAB solver. **Fig. 3 E** highlights a substantial increase in MSE at short scales (<10) and a more moderate increase at long scales (>10). **Fig. 3 F** presents the PSD distribution, showing an increase across all frequencies, particularly in the LF and very-LF ranges.

Comparison to experimental results

We compared the BIV predictions of our model—denoted as "int" since stochasticity was introduced into the intrinsic mechanisms of the model—with BIV data from mouse SAN patch-clamp experiments (22,23). We also compared our

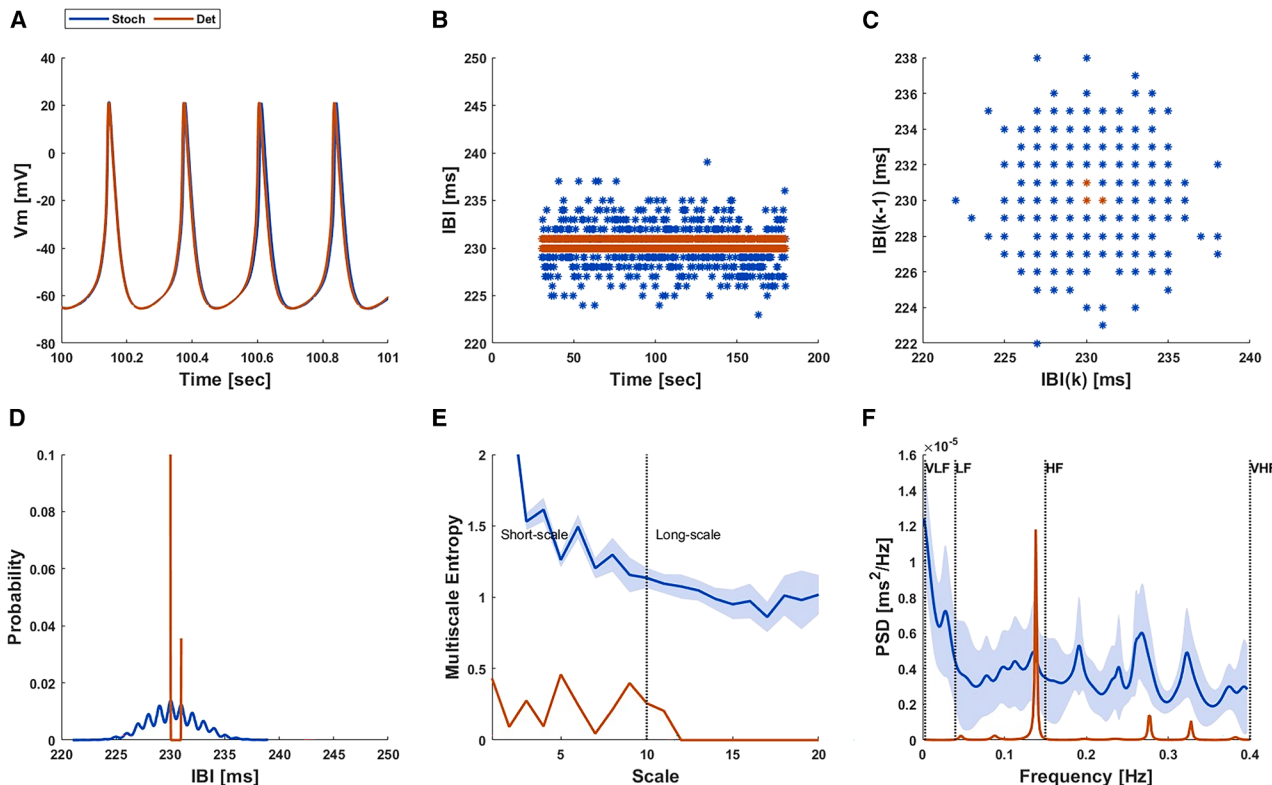


FIGURE 3 (A) A representative membrane potential for both the deterministic (red) and stochastic (blue) models. (B) The calculated interbeat intervals (IBIs) from the same representative sample. (C) The Poincaré plot of these representative samples. (D) Mean histograms of the stochastic and deterministic models with 95% two-sided confidence intervals. (E) Multiscale entropy analysis of both models with 95% two-sided confidence intervals. (F) Power spectral density analysis across all frequencies with 95% two-sided confidence intervals.

model to a basic stochastic model, in which white noise was added directly to the membrane potential—denoted as "out" since the noise was applied to the model's output.

Fig. 4 compares IBI distributions obtained from experimental data, the deterministic model, a basic stochastic model, and our novel stochastic model. KSTs confirmed that the IBI distribution generated by our stochastic model aligns most closely with the experimental data, significantly outperforming both the deterministic and basic stochastic models. Although no substantial difference in overall variability was observed when comparing our model to the basic stochastic model (**Fig. 4, B and F**), our model showed a marked improvement in the PSD (**Fig. 4 D**), indicating better capture of the underlying temporal dynamics. Whereas our model showed significant improvements in short- and long-scale entropy compared to the deterministic model, the difference from the basic stochastic model was moderate and focused mainly on the long-scale entropy (**Fig. 4 C**).

The IBI distributions of both the deterministic and stochastic models were evaluated against the experimental data using the KST. The stochastic model's distribution showed a significantly smaller distance from the experimental data ($p < 0.0001$) than the deterministic model, as confirmed by a permutation test applied to the KST results.

This statistical test was also used to compare the basic stochastic model to our stochastic model, revealing a significant improvement ($p < 0.0001$) in our model.

Response to β -AR stimulation

We simulated the effect of β -AR stimulation on the IBI distribution using varying concentrations of the nonspecific β -AR stimulator, ISO. **Fig. 5 A** shows a representative IBI distribution, highlighting the decrease in both the average IBI and SD as the ISO concentration increases. **Fig. 5 B** presents histograms from all simulations of each specific model configuration, similarly showing the reduction in the average IBI and SD with increasing ISO concentrations. **Fig. 5 C** displays the MSE curves for both the deterministic and stochastic models for 20 scales, before and after the application of ISO, showing no apparent effect of ISO on MSE at short (<10) scales and a moderate increase at long (>10) scales. **Fig. 5 D** illustrates the impact of ISO stimulation on PSD levels, revealing a moderate decreased LF component as the ISO concentration increases. **Fig. 5 E** demonstrates that increasing ISO concentrations shortened the average IBI, whereas **Fig. 5 F** shows a corresponding decrease in the coefficient of variance (CV) of the IBIs with increasing ISO concentrations.

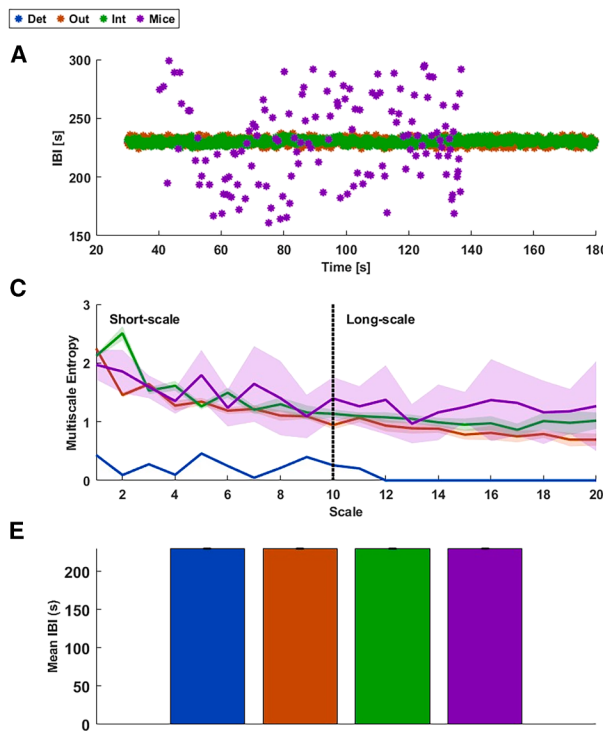


FIGURE 4 A comparison between our model (green), denoted as "int" since stochasticity was introduced into the intrinsic mechanisms of the model, and interbeat interval variability (BIV) data from mouse SAN patch-clamp experiments (purple). The comparison also includes the deterministic model (blue) and a basic stochastic model (red), in which white noise was added directly to the membrane potential—denoted as "out" since the noise was applied to the model's output. (A) A representative sample from each model, showing the calculated interbeat intervals (IBIs). (B) Mean histograms of all models with 95% two-sided confidence intervals. (C) Multiscale entropy analysis of all models with 95% two-sided confidence intervals. (D) Power spectral density analysis across all frequencies with 95% two-sided confidence intervals. (E) The mean IBI derived from each model, with error bars representing ± 1 standard deviation. (F) The coefficient of variance of the IBIs, also shown with error bars indicating ± 1 standard deviation.

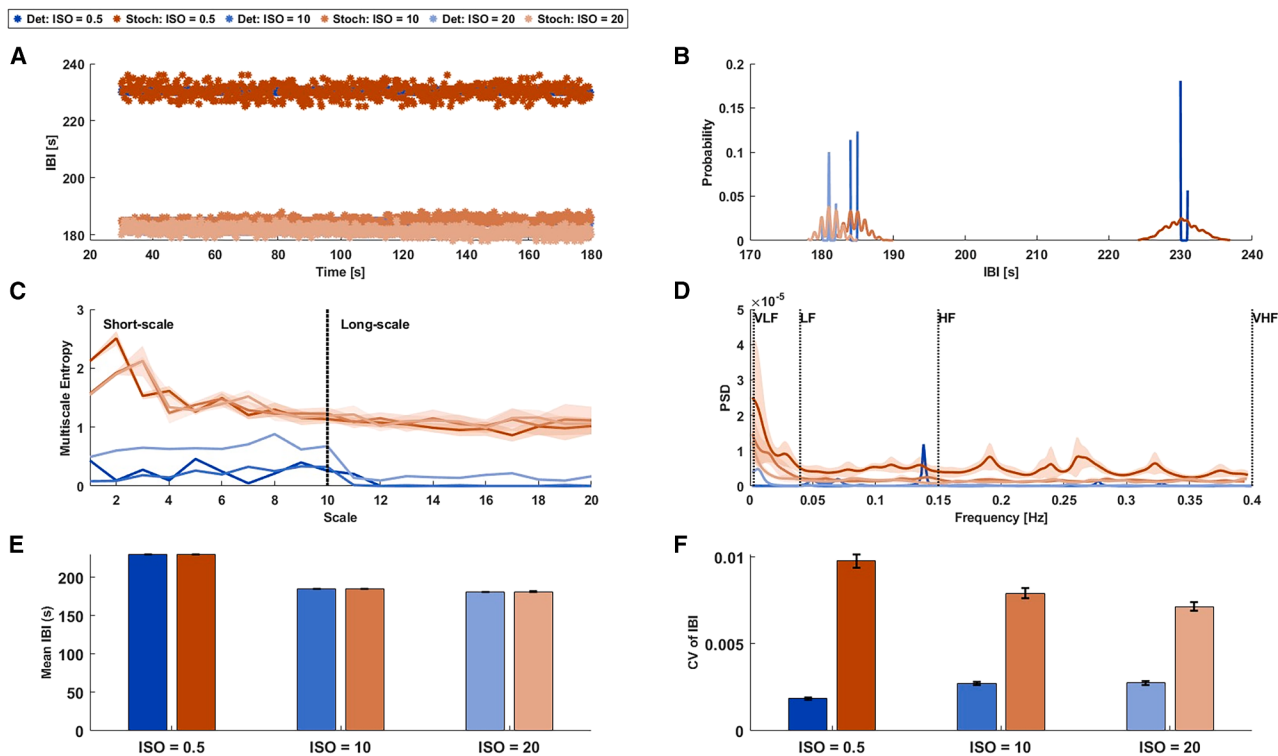


FIGURE 5 Simulation of the deterministic (shades of blue) and stochastic (shades of red) models in response to β -adrenergic stimulation. (A) A representative sample from each model, showing the calculated interbeat intervals (IBIs) in response to 0.5 (dark shade), 10 (medium shade), and 20 (light shade) nM isoproterenol (ISO). (B) Mean histograms of all models with 95% two-sided confidence intervals. (C) Multiscale entropy analysis of all models with 95% two-sided confidence intervals. (D) Power spectral density analysis across all frequencies with 95% two-sided confidence intervals. (E) The mean IBI derived from each model, with error bars representing ± 1 standard deviation. (F) The coefficient of variance of the IBIs, also shown with error bars indicating ± 1 standard deviation.

Response to PDE inhibition

We simulated the effect of PDE stimulation on the IBI distribution by adding different concentrations of 3-isobutyl-1-methylxanthine (IBMX). Fig. 6 A shows a representative IBI distribution, highlighting the decrease in both the average IBI and SD as the IBMX concentration increases. Fig. 6 B presents histograms from all simulations of each specific model configuration, similarly showing the reduction in average IBI and SD with increasing IBMX concentrations. Fig. 6 C displays the MSE curves for both the deterministic and stochastic models across 20 scales, before and after the application of IBMX, showing that higher levels of stimulation increased entropy at long scales but had no apparent impact on the short scales. Fig. 6 D illustrates the impact of IBMX on PSD levels, revealing a decrease in LF components while applying IBMX, with no apparent difference between the tested concentrations. Fig. 6 E demonstrates that increasing IBMX concentrations shortened the average IBI, whereas Fig. 6 F shows that high concentrations of IBMX resulted in a reduced CV of the IBIs.

Response to SERCA upregulation

We simulated the effect of SERCA regulation on the IBI distribution using different activation levels of SERCA, reflect-

ing mutations that increase SERCA activity. Fig. 7 A shows a representative IBI distribution, highlighting the decrease in both the average IBI and SD as SERCA activation increases. Fig. 7 B presents histograms from all simulations of each specific model configuration, similarly showing reductions in the average IBI and SD with increasing SERCA activation. Fig. 7 C displays the MSE curves for both the deterministic and stochastic models across 20 scales at distinct SERCA activation levels. Higher activation levels decreased entropy at short scales (<2) while increasing it at intermediate and long scales (6 < scale). Fig. 7 D illustrates the impact of SERCA activation on PSD levels, showing a significant decrease in all frequencies for both overactivated configurations, with no apparent differences between the two overactivated conditions. Fig. 7 E demonstrates that increasing SERCA activation shortened the average IBI, whereas Fig. 7 F shows that overactivated SERCA reduced CV, with no significant difference observed between the two overactivated conditions.

DISCUSSION

The present study investigated the effect of the stochasticity of internal pacemaker mechanisms on BIV of mouse SANCs. The AP pattern of our stochastic coupled-clock model

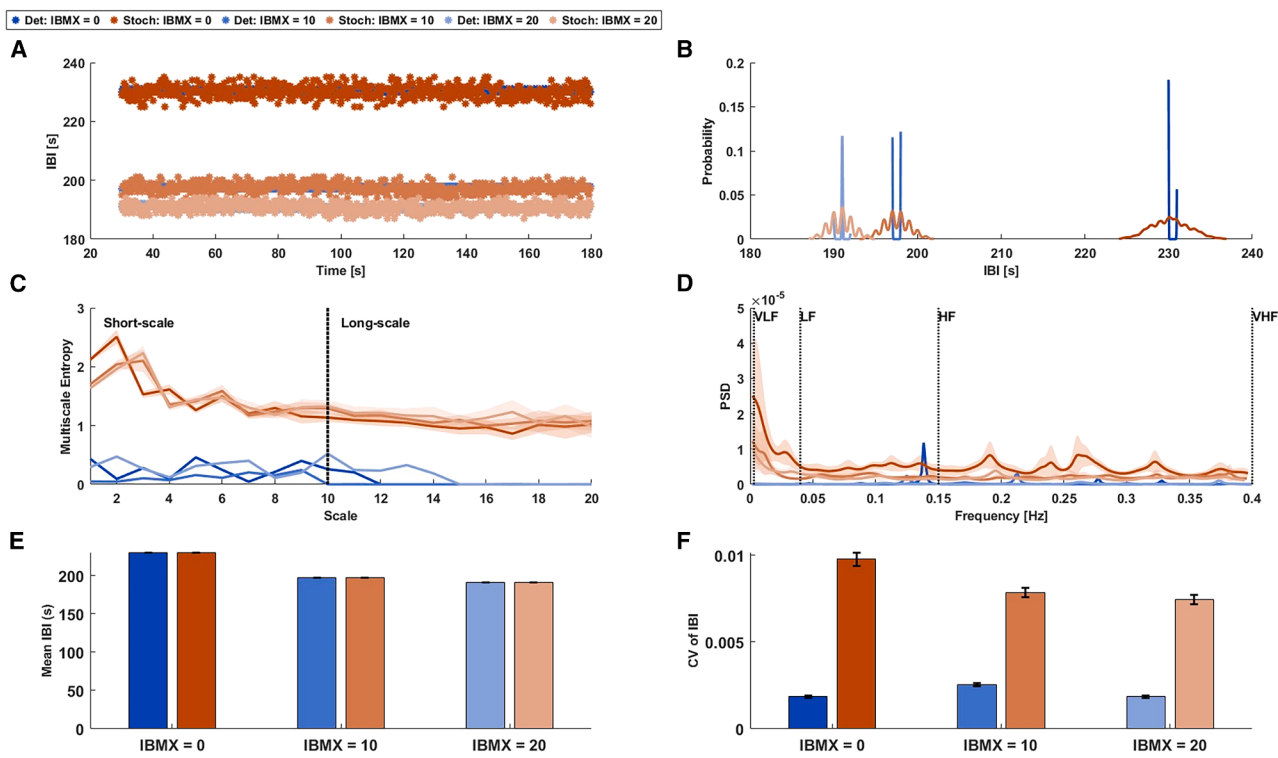


FIGURE 6 Simulation of the deterministic (shades of blue) and stochastic (shades of red) models in response to phosphodiesterase (PDE) inhibition. (A) A representative sample from each model, showing the calculated interbeat intervals (IBIs) in response to 0 (dark shade), 10 (medium shade), and 20 (light shade) μM IBMX. (B) Mean histograms of all models with 95% two-sided confidence intervals. (C) Multiscale entropy analysis of all models with 95% two-sided confidence intervals. (D) Power spectral density analysis across all frequencies with 95% two-sided confidence intervals. (E) The mean IBI derived from each model, with error bars representing ± 1 standard deviation. (F) The coefficient of variance of the IBIs, also shown with error bars indicating ± 1 standard deviation.

exhibited noise behavior similar to that observed in experimental results, thereby supporting the first hypothesis that integrating stochastic behavior into intrinsic mechanisms mimics experimental BIV. Introducing stochasticity to each individual coupled-clock mechanism revealed that the RyR stochasticity contributed equally to short- and long-scale entropy, whereas ANS stochasticity increased mainly long-scale entropy and added LFs. In contrast, the L-type calcium channels and funny channel effects were relatively moderate.

In response to β -AR activation, PDE inhibition, or increased SERCA activation, the IBI was shortened alongside a reduction in SD, supporting the second hypothesis. Increased β -AR activation led to a moderate reduction in LFs and very LFs and an increase in the long-scale entropy. Increased PDE inhibition led to more prominent reduction in the LFs and an increase in entropy at intermediate and long scales ($8 < \text{scale} < 8$) but led to no change in short-scales ($4 < \text{scale} < 8$), whereas increased SERCA activity increased the entropy in all scales, apart from a decrease at the very short scales ($\text{scale} < 2$), thereby supporting the third hypothesis that drugs/mutations have distinct effects on BIV parameters in long and short scales. Increased β -AR activation or PDE inhibition enhances the activity of the AC-cAMP/PKA signaling cascade at different components of the cascade (that have different inherent noise distributions),

resulting in stronger coupling of the coupled-clock system and thereby influencing channel activities (24). Additionally, increased SERCA activity elevates intracellular Ca^{2+} levels, which further activates the AC-cAMP/PKA cascade, also promoting greater coupling of the coupled-clock system. Although these drugs shorten the IBI, they all contribute to increased entropy by amplifying the activity magnitude of different coupled-clock mechanisms.

Alternative stochastic models of the coupled-clock model have been proposed (13). However, in these models, stochasticity was introduced directly into the AP itself (output) rather than within the mechanisms leading to the AP. The current study aimed to capture more physiological phenomena and simulate the effects of drugs on BIV by incorporating stochasticity into the intrinsic mechanisms. It is worth noting that even when stochasticity was introduced into the coupled-clock mechanisms rather than directly into the AP, the resulting IBI series exhibited pink noise patterns similar to experimental findings.

In our model, we did not introduce generic random variables into intrinsic cellular mechanisms; instead, we applied physiologically informed stochasticity. Initially, we investigated the relationship between different noise spectral profiles and specific cellular processes. White Gaussian noise was employed for intrinsic channels, such as the funny

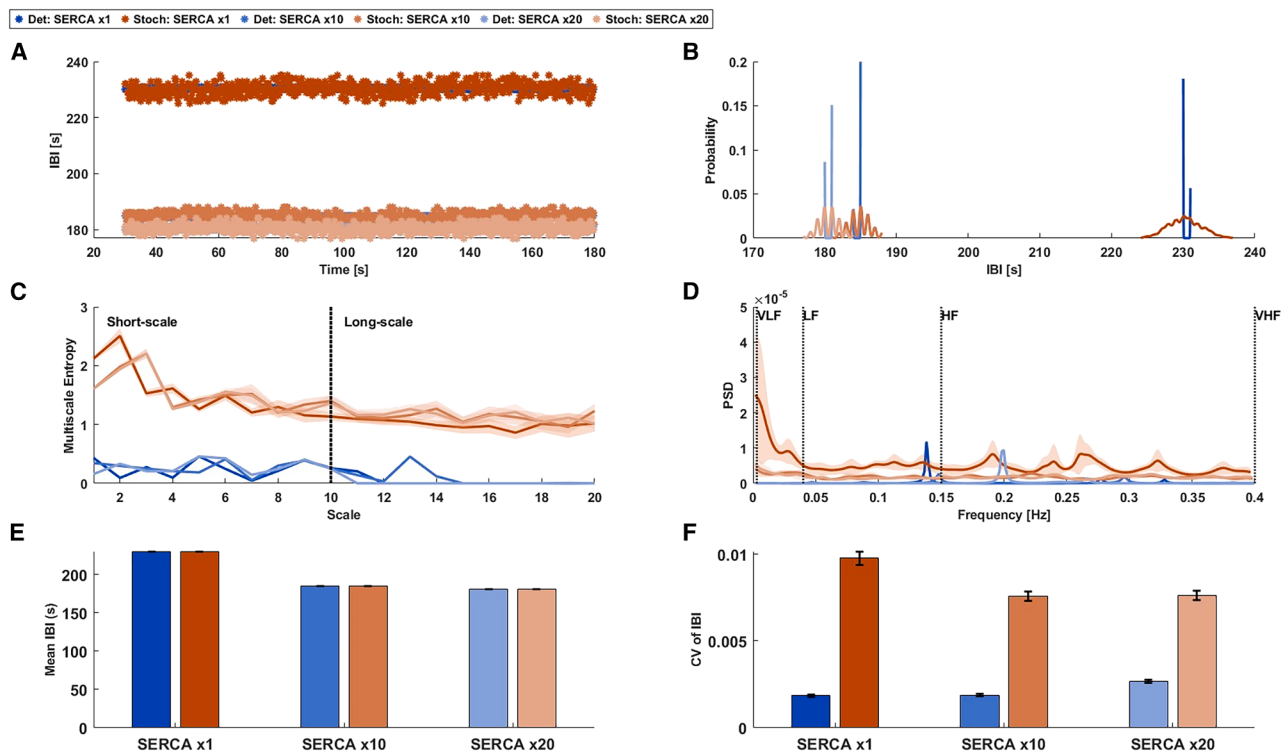


FIGURE 7 Simulation of the stochastic model in response to increased SERCA activity. (A) A representative sample from each model, showing the calculated interbeat intervals (IBIs) in response to $1\times$ (dark shade), $10\times$ (medium shade), and $20\times$ (light shade) activation levels of the SERCA channel. (B) Mean histograms of all models with 95% two-sided confidence intervals. (C) Multiscale entropy analysis of all models with 95% two-sided confidence intervals. (D) Power spectral density analysis across all frequencies with 95% two-sided confidence intervals. (E) The mean IBI derived from each model, with error bars representing ± 1 standard deviation. (F) The coefficient of variance of the IBIs, also shown with error bars indicating ± 1 standard deviation.

current, RyR gating, and Ca^{2+} channels, based on the framework introduced by Fox et al. (15), which justifies using white noise to represent stochastic channel gating arising from finite channel numbers. In contrast, autonomic inputs (ISO and CCh) were modeled using spectrally shaped pink noise, following a method conceptually adapted from Rosenberg et al. (16), with LF components dominating ISO fluctuations and HF components shaping CCh inputs.

Each noise signal was initially scaled to have a standard deviation approximately two orders of magnitude smaller than the mean of the affected variable and then empirically tuned based on comparison with experimental recordings. Among the various sources, the most influential on BIV were fluctuations in the RyR function and ISO levels, each contributing distinct temporal patterns. Together, these components interact to produce the observed complexity and variability in SAN pacing behavior.

The model predicted that in response to β -AR activation or PDE inhibition, IBI is shortened and SD is decreased. These findings align with a reduction in BIV documented previously after β -AR activation (25). Additionally, when SERCA activity was reduced, the IBI became irregular, consistent with experimental results reported previously (26). When SERCA activity increased, the IBI was shortened with a decrease in SD, mirroring the effects observed

with other drugs. However, despite the similarities in their effects on IBI and SD, their short- and long-scale entropy were different, as well as the effect on the LFs. These findings align with reports of a decrease in LFs in response to IBMX in mouse SAN tissue (27).

HRV provides insights into the autonomic regulation of cardiac function (28). IBI not only reflects the heart's rhythm but also signifies the balance of physiological processes critical for cardiovascular health. Therefore, measurements of HRV and IBI play a vital role in assessing stress levels, cardiovascular health, and overall physiological well-being. Understanding the mechanisms contributing to BIV and how they are influenced by nervous system receptor stimulation represents the initial step toward characterizing the underlying mechanisms of HRV.

Limitations

The stochastic parameters in our model were chosen empirically and have not been experimentally measured, as precise measurement is not applicable. The stochasticity of Ca^{2+} release from the SR was modeled solely through RyR gating, without modeling direct currents. Additionally, our “common pool” approach represents average ion concentrations, thereby ignoring local channel interactions

and single-channel currents. Furthermore, the study focused on a SAN cell, whereas intact SAN tissue exhibits smaller BIV than isolated cells, and single cells from the same SAN can display a broader range of beating rates.

DATA AND CODE AVAILABILITY

All codes are available at <https://bioelectric-bioenergetic-lab.net.technion.ac.il/upon/publications>.

ACKNOWLEDGMENTS

This research was funded by ISF 1230/24 (Y.Y.) and Kamin (Y.Y.) and was supported by the Rambam-Atidim Academic Excellence Program (I.W.-B.). The authors did not use generative AI or AI-assisted technologies in the development of this manuscript.

AUTHOR CONTRIBUTIONS

Y.Y. and I.W.-B. designed the research, N.A. performed research and analyzed data, and Y.Y. and N.A. wrote the manuscript.

DECLARATION OF INTERESTS

The authors declare no competing interests.

SUPPORTING MATERIAL

Supporting material can be found online at <https://doi.org/10.1016/j.bjpn.2025.07.031>.

REFERENCES

- Abdelsayed, M., E. J. Kort, ..., M. Mercola. 2022. Repurposing drugs to treat cardiovascular disease in the era of precision medicine. *Nat. Rev. Cardiol.* 19:751–764.
- Costa, M., A. L. Goldberger, and C.-K. Peng. 2005. Multiscale entropy analysis of biological signals. *Phys. Rev. E.* 71:021906.
- Yaniv, Y., K. Tsutsui, and E. G. Lakatta. 2015. Potential effects of intrinsic heart pacemaker cell mechanisms on dysrhythmic cardiac action potential firing. *Front. Physiol.* 6:47.
- Yaniv, Y., E. G. Lakatta, and V. A. Maltsev. 2015. From two competing oscillators to one coupled-clock pacemaker cell system. *Front. Physiol.* 6:28.
- Lakatta, E. G., V. A. Maltsev, and T. M. Vinogradova. 2010. A coupled SYSTEM of intracellular Ca^{2+} clocks and surface membrane voltage clocks controls the timekeeping mechanism of the heart's pacemaker. *Circ. Res.* 106:659–673.
- Adair, R. K. 2003. Noise and stochastic resonance in voltage-gated ion channels. *Proc. Natl. Acad. Sci. USA.* 100:12099–12104.
- Yang, H., and M. A. Xu-Friedman. 2013. Stochastic properties of neurotransmitter release expand the dynamic range of synapses. *J. Neurosci.* 33:14406–14416.
- Wilders, R., and H. J. Jongsma. 1993. Beating irregularity of single pacemaker cells isolated from the rabbit sinoatrial node. *Biophys. J.* 65:2601–2613.
- Zaza, A., and F. Lombardi. 2001. Autonomic indexes based on the analysis of heart rate variability: a view from the sinus node. *Cardiovasc. Res.* 50:434–442.
- Vinogradova, T. M., and E. G. Lakatta. 2021. Dual Activation of Phosphodiesterase 3 and 4 Regulates Basal Cardiac Pacemaker Function and Beyond. *Int. J. Mol. Sci.* 22:8414.
- Yaniv, Y., I. Ahmet, ..., E. G. Lakatta. 2014. Synchronization of sino-atrial node pacemaker cell clocks and its autonomic modulation impart complexity to heart beating intervals. *Heart Rhythm.* 11:1210–1219.
- Arbel-Ganon, L., J. A. Behar, ..., Y. Yaniv. 2020. Distinct mechanisms mediate pacemaker dysfunction associated with catecholaminergic polymorphic ventricular tachycardia mutations: Insights from computational modeling. *J. Mol. Cell. Cardiol.* 143:85–95.
- Dvir, H., and S. Zlochiver. 2015. Interbeat Interval Modulation in the Sinoatrial Node as a Result of Membrane Current Stochasticity—A Theoretical and Numerical Study. *Biophys. J.* 108:1281–1292.
- Maltsev, A. V., O. Monfredi, and V. A. Maltsev. 2022. Universal Inverse-Square Relationship Between Heart Rate Variability and Heart Rate Originating in Cardiac Pacemaker Cells. *JACC. Clin. Electrophysiol.* 8:1042–1044.
- Fox, R. F. 1997. Stochastic versions of the Hodgkin-Huxley equations. *Biophys. J.* 72:2068–2074.
- Rosenberg, A. A., I. Weiser-Bitoun, ..., Y. Yaniv. 2020. Signatures of the autonomic nervous system and the heart's pacemaker cells in canine electrocardiograms and their applications to humans. *Sci. Rep.* 10:9971.
- Yaniv, Y., I. Ahmet, ..., E. G. Lakatta. 2016. Deterioration of autonomic neuronal receptor signaling and mechanisms intrinsic to heart pacemaker cells contribute to age-associated alterations in heart rate variability in vivo. *Aging Cell.* 15:716–724.
- Kharche, S., J. Yu, ..., H. Zhang. 2011. A mathematical model of action potentials of mouse sinoatrial node cells with molecular bases. *Am. J. Physiol. Circ. Physiol.* 301:H945–H963.
- Yaniv, Y., A. Ganesan, ..., E. G. Lakatta. 2014. Parallel increase in PKA activation kinetics and spontaneous beating rate in sinoatrial node cell in response to chronotropic stimuli. *Heart Rhythm.* 11:S164.
- Behar, J., and Y. Yaniv. 2017. Age-related pacemaker deterioration is due to impaired intracellular and membrane mechanisms: Insights from numerical modeling. *J. Gen. Physiol.* 149:935–949.
- Behar, J. A., A. A. Rosenberg, ..., Y. Yaniv. 2018. PhysioZoo: A novel open access platform for heart rate variability analysis of mammalian electrocardiographic data. *Front. Physiol.* 9:1390.
- Ren, L., P. N. Thai, and N. Chiamvimonvat. 2022. Adenylyl cyclase isoform 1 contributes to sinoatrial node automaticity via functional microdomains. *JCI Insight.* 7:e162602.
- Reddy, G. R., L. Ren, ..., M. F. Navedo. 2021. Deciphering cellular signals in adult mouse sinoatrial node cells. *iScience.* 25:103693.
- Behar, J., A. Ganesan, ..., Y. Yaniv. 2016. The autonomic nervous system regulates the heart rate through cAMP-PKA dependent and independent coupled-clock pacemaker cell mechanisms. *Front. Physiol.* 7:419.
- Yang, D., C. H. Morrell, ..., E. G. Lakatta. 2021. Ca^{2+} and Membrane Potential Transitions During Action Potentials Are Self-Similar to Each Other and to Variability of AP Firing Intervals Across the Broad Physiologic Range of AP Intervals During Autonomic Receptor Stimulation. *Front. Physiol.* 12:612770.
- Yaniv, Y., A. E. Lyashkov, ..., E. G. Lakatta. 2014. Stochasticity intrinsic to coupled-clock mechanisms underlies beat-to-beat variability of spontaneous action potential firing in sinoatrial node pacemaker cells. *J. Mol. Cell. Cardiol.* 77:1–10.
- Shemla, O., K. Tsutsui, ..., Y. Yaniv. 2020. Beating rate variability of isolated mammal sinoatrial node tissue: insight into its contribution to heart rate variability. *Front. Neurosci.* 14:614141.
- Yaniv, Y., and E. G. Lakatta. 2013. Pacemaker gene mutations, bradycardia, arrhythmias and the coupled clock theory. *J. Cardiovasc. Electrophysiol.* 24:E28–E29.